

# In Situ Transmission Electron Microscopy for Ultrahigh Temperature Mechanical Testing of ZrO<sub>2</sub>

Robson L. Grosso, Eliana N. S. Muccillo, Dereck N. F. Muche, Gowtham S. Jawaharram, Christopher M. Barr, Anthony M. Monterrosa, Ricardo H. R. Castro, Khalid Hattar,\* and Shen J. Dillon\*

Cite This: *Nano Lett.* 2020, 20, 1041–1046

Read Online

ACCESS |

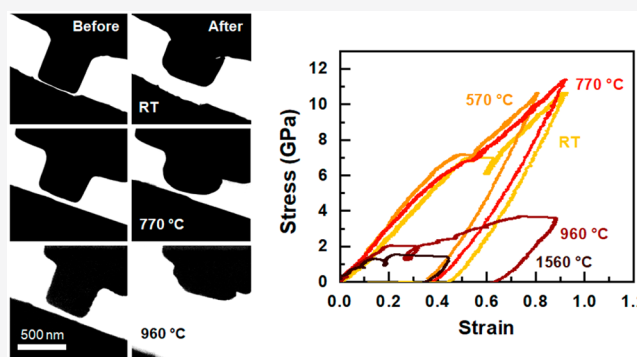
Metrics & More

Article Recommendations

Supporting Information

**ABSTRACT:** This work demonstrates a novel approach to ultrahigh-temperature mechanical testing using a combination of in situ nanomechanical testing and localized laser heating. The methodology is applied to characterizing and testing initially nanograined 10 mol % Sc<sub>2</sub>O<sub>3</sub>-stabilized ZrO<sub>2</sub> up to its melting temperature. The results suggest that the low-temperature strength of nanograined,  $d < 50$  nm, oxides is not influenced by creep. Tensile fracture of ZrO<sub>2</sub> bicrystals produce a weak-temperature dependence suggesting that grain boundary energy dominates brittle fracture of grain boundaries even at high homologous temperatures; for example,  $T = 2050$  °C or  $T \approx 77\% T_{\text{melt}}$ . The maximum temperature for mechanical testing in this work is primarily limited by the instability of the sample, due to evaporation or melting, enabling a host of new opportunities for testing materials in the ultrahigh-temperature regime.

**KEYWORDS:** *In situ*, Transmission electron microscopy, Ultrahigh temperature, Nanomechanical testing, Nanocrystalline, Grain boundary



High-temperature structural materials optimized for use in extreme environments perform critical roles in energy conversion, aerospace applications, and civil defense.<sup>1–3</sup> The lack of suitable structural materials stable in extreme environments, particularly at high temperatures and in reactive environments, is a key limitation in many related systems. Several key factors constrain the rate of development of novel structural materials for ultrahigh-temperature applications, for example,  $T > 2000$  °C, including materials processing and challenges for ultrahigh-temperature materials metrology. Ultrahigh-temperature mechanical testing either requires highly specialized instrumentation or has limitations on mechanical testing modes.<sup>4–8</sup> The limited ability to mechanically test materials in the ultrahigh-temperature regime constrains our understanding of creep deformation, diffusion, and thermodynamics in ultrahigh-temperature materials as well as geological materials. When developing novel materials, such as nanostructured samples, new high entropy ultrahigh-temperature materials or novel composites, producing highly dense macroscopic samples suitable for bulk testing can be challenging, especially since most ultrahigh-temperature materials tend to be brittle and extremely flaw sensitive.<sup>9,10</sup> In recent decades, microscale and nanoscale mechanical testing have provided great insights into deformation mechanisms in numerous materials and have facilitated characterization of samples prepared in small volumes, such as thin films,

whiskers, and single nanoparticles.<sup>11–13</sup> When coupled with in situ imaging and diffraction, the deformation pathways may be observed directly.<sup>14,15</sup> Commercially available nanomechanical testing platforms can heat to  $\approx 800$  °C.<sup>16–18</sup> Specialized in situ microscale experiments have tested samples up to 1150 °C.<sup>19–21</sup> However, extending to the ultrahigh-temperature regime ( $T > 2000$  °C) relevant to extreme environments has to date not been possible. For example, ZrO<sub>2</sub> melts at 2715 °C and testing at  $T > 3/4 T_m$  requires access to the ultrahigh-temperature regime. The mechanical properties of ZrO<sub>2</sub> are of interest over a broad temperature range as they relate to fuel cells ( $T \approx 800$  °C), thermal barrier coatings ( $T > 1300$  °C), and the surface oxides on ZrC in ultrahigh-temperature conditions ( $T > 2000$  °C).<sup>22–24</sup>

In this work, we seek to characterize the mechanical properties of initially dense nanograined 10 mol % Sc<sub>2</sub>O<sub>3</sub>-stabilized ZrO<sub>2</sub> (10ScSZ) over a broad range of temperatures relevant to its various applications in fuel cells, high-temperature structural materials, and thermal barrier coatings. The similarity in ionic radii of Sc<sup>3+</sup> (0.87 Å) and Zr<sup>4+</sup> (0.84 Å)

**Received:** October 11, 2019

**Revised:** January 8, 2020

**Published:** January 13, 2020

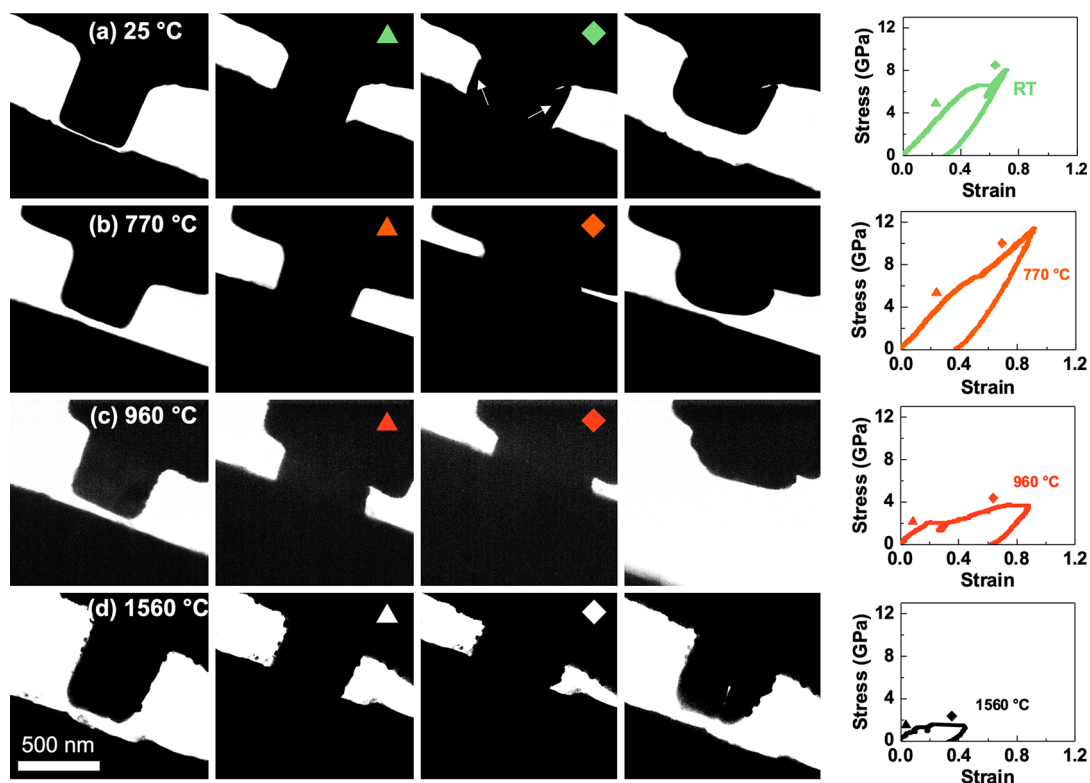


**Figure 1.** Time-lapse images of in situ TEM nanopillar compression testing with the associated engineering stress–strain curve at different temperatures: (a) 25, (b) 770, (c) 960, and (d) 1560 °C. Symbols indicate the specific point in the stress–strain curve where the images were recorded. Arrows indicate shear directions in the room-temperature experiments where cracking is observed.

confers it with the highest ionic conductivity and defect association enthalpy among  $\text{ZrO}_2$ -based oxides,<sup>25</sup> which has generated interest in 10ScSZ.<sup>26,27</sup> Nanograined  $\text{ZrO}_2$  exhibits considerable strengthening relative to its coarse-grained counterparts. For nanograined oxides where the grain size  $d < 50$  nm, there has been debate regarding the extent to which grain boundary diffusion could contribute to plasticity, even at low temperatures. Such mechanisms have been proposed to explain the so-called inverse Hall-Petch behavior observed in certain ceramics.<sup>28,29</sup> Supporting Information (SI) Figure S1 shows the grain size,  $d$ , dependence of yield strength measured from 10ScSZ nanopillars, which demonstrates an increase in hardness for  $d < 50$  nm that is consistent with Hall-Petch like scaling and the onset of inverse Hall-Petch response for  $d < 15$  nm. Extrapolation of high-temperature diffusivity values to room temperature do not support claims of diffusion-mediated room-temperature creep. Those measurements suggest that the room-temperature creep rate of a  $d = 10$  nm cubic  $\text{ZrO}_2$  would be at most  $\approx 10^{-15} \text{ s}^{-1}$  and as low as  $\approx 10^{-60} \text{ s}^{-1}$ ; see SI Figure S2. It could be argued that the grain boundary structures in these nanograined samples are inherently different than in coarse grain samples that cause their diffusivity to differ from their coarse grain analogues. The strain rates associated with sintering of the samples tested herein, however, generally agree in magnitude with creep rates predicted from measurements of high-temperature cation grain boundary diffusivity; see SI Figure S2. Recent micropillar compression experiments performed on nanograined  $\text{ZrO}_2$  up to  $T = 600$  °C demonstrated considerable softening by  $T = 400$  °C.<sup>30</sup> This response might, however, be attributed to a combination of point and line defects induced by the flash sintering process and residual porosity observable in those materials.<sup>30</sup> Nano-

grained  $\text{ZrO}_2$  may be sintered under applied pressure at temperatures as low as  $T \approx 700$  °C.<sup>31</sup> 10ScSZ retains its nanograin structure to  $T \approx 950$  °C, thus it is possible to test the temperature dependence of dense 10ScSZ across the range of temperatures where grain boundary diffusion is potentially active. Nanomechanical testing to  $T > 950$  °C, that is, the onset of measurable grain growth, requires a new strategy for sample heating that extends beyond the range of existing solutions.

Laser heating provides an effective route to obtaining local heating to extremely high temperatures, while maintaining low temperatures in the vicinal region.<sup>32</sup> The general approach allows one to take advantage of various existing high precision nanomechanical testing methodologies. Performing experiments in situ within a transmission electron microscope (TEM) enables characterization of deformation modes as well as utilization of electron diffraction for local temperature determination. Here, we demonstrate laser heating of 10ScSZ on a commercial nanomechanical testing platform to its melting temperature and in situ TEM-based mechanical testing to  $T = 2050$  °C.

Single crystal 8 mol %  $\text{Y}_2\text{O}_3$ -stabilized  $\text{ZrO}_2$  (8YSZ) was selected as an indenter since it has low thermal conductivity and reasonably matches the thermal impedance and optical absorption of 10ScSZ. These factors favor temperature uniformity. The main drawback of this material is that its elastic compliance and strength are also similar to the test specimen. However, due to the significant hydrostatic stress component in the large indenter, as compared to the nanopillar, yielding is anticipated to occur primarily in the pillar in agreement with three-dimensional finite element simulations presented in SI Figure S3. Electron diffraction

provides a means for temperature determination via strain in the lattice parameter as detailed in ref 33. SI Figure S4 shows example electron diffraction patterns at different laser powers obtained from a single large grain grown by preannealing, as well as a temperature calibration curve. Nanograined 10ScSZ remains cubic at both room temperature and high temperatures but coarse-grained 10ScSZ transforms reversibly to the rhombohedral ( $\beta$ ) phase at  $\sim 525$  °C.<sup>34</sup> Thus,  $\beta$ -phase exists in the diffraction pattern in preannealed samples below 525 °C. The applied laser power versus temperature is approximately linear just beyond a threshold applied power of  $P > 1.5$  W. The onset of grain growth, the  $\beta$  to cubic phase transition in precoarsened grains, the onset of thermal instability in the pillars, and the melting temperature of 10ScSZ were all utilized as secondary reference points to validate the calibration. The fit curve was weighted by the phase transition temperatures.

Figure 1 shows time lapse images of nanopillars compressed at  $5 \text{ nm s}^{-1}$  at different temperatures, as well as associated stress–strain curves. The engineering stress–strain curves obtained during the compression testing can be seen in SI Figure S5. At room temperature, the yield strength of as-prepared nanograined cubic 10ScSZ samples is  $6.5 \pm 0.6$  GPa, whereas preannealed single crystalline  $\text{Sc}_2\text{O}_3$ -doped  $\beta$ - $\text{ZrO}_2$  ( $\beta$ -10ScZ) samples of random grain orientation have compressive yield strengths of  $2.2 \pm 0.4$  GPa. The yield strengths were all determined from the point at which the stress–strain response deviates from the average linear response. At room temperature, the 10ScSZ samples tend to fail via fracture along directions of maximum resolved shear, as indicated by the arrows in Figure 1a, that results in large discontinuities in the measured stress–strain curves. As temperature increases, the magnitudes of the strain discontinuities decrease and cracking becomes less observable. By  $T = 770$  °C, the samples deform relatively uniformly without evidence of cracks in the images or associated displacement discontinuities in the stress–strain curves. Figure 2 plots the yield strength versus temperature for the samples tested in this study. The yield strength decreases considerably between 770 and 960 °C. Within this temperature range, the onset of grain growth occurs, which is shown in SI Figure S6. The coarsening likely accounts for much of the reduction in strength. To support this hypothesis, samples

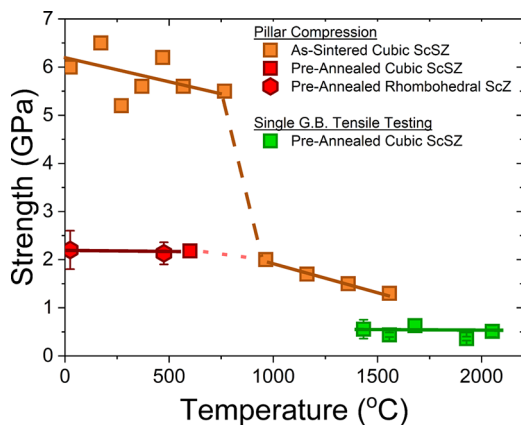


**Figure 2.** Strength as a function of temperature for the as-prepared nanograined 10ScSZ and preannealed 10ScSZ tested by pillar compression along with data for single grain boundary fracture measured under tension. For pillar compression experiments, the yield strength is reported; for single grain boundary tensile tests, the fracture strength is reported.

were preannealed at high temperature and then tested at lower temperature. Preannealing was performed by using in situ laser irradiation and new pillars were then prepared from those regions and subsequently mechanically tested at high temperature. Because of the  $\beta$ -to-cubic phase transition occurring in preannealed samples, it is not possible to test coarse grain cubic 10ScSZ at room temperature in order to isolate the grain size and temperature effects. Instead, cubic 10ScSZ is tested just above the  $\beta$ -to-cubic phase transition temperature and compared with coarse grain  $\beta$ -10ScZ just below the transition temperature. At 575 °C, the yield strength of preannealed 10ScSZ aligns with values extrapolated from  $T > 960$  °C. The preannealed  $\beta$ -10ScZ has approximately the same yield strengths at 475 °C and room temperature which are comparable to values obtained from cubic 10ScSZ at 575 °C. All coarse-grain samples exhibit significantly lower yield strength, regardless of temperature, than the nanograin samples, which indicate that grain size is the primary cause for the reduction in strength observed at  $T \geq 960$  °C. Below and above this temperature interval, the yield strength varies weakly with temperature on average decreasing about 1.1 and 1.2 MPa  $\text{K}^{-1}$ , respectively. The weak-temperature dependence below 770 °C suggests that grain boundary diffusion does not contribute appreciably to plasticity in our samples tested at strain rates of  $\sim 10^{-2} \text{ s}^{-1}$ , since they would then follow Arrhenius behavior consistent with Coble creep (activation enthalpy  $\sim 370 \text{ kJ mol}^{-1}$ ).<sup>35</sup> As noted in SI Figure S2, the sintering strain rate of  $d = 10 \text{ nm}$  samples reaches  $10^{-3} \text{ s}^{-1}$  at 700 °C, which is consistent with our results. It also supports the claim that Coble creep can not be active in our samples at room temperature on measurable time scales.

Nanoindentation-based measurements produce a modulus of  $E = 208 \pm 6$  GPa for the as-prepared samples. Pillar compressions performed on the same material using a diamond indenter produce an apparent modulus of  $E = 78 \pm 13$  GPa, which is common when the compliance of the tip and substrate is not accounted for; see SI Figure S7. A correction factor based on elastic finite element modeling, similar to those shown in SI Figure S3, predicts a sample modulus  $E = 123$  GPa. Compression of pillars with the YSZ indenter further reduces the apparent modulus to  $E = 24$  GPa measured during unloading. Using FEM to correct the apparent modulus measured during unloading produces a value of  $E = 96$  GPa. Pillar bending, stress localization near the loading contact, hydrostatic stresses due to the boundary conditions, and other geometric nonidealities can strongly influence the apparent modulus measured from nanopillar compression.<sup>36</sup> The factor of two difference between this value and the nominal value could arise from these geometric nonidealities. As shown in SI Figure S8, the apparent modulus decreases with increasing temperature.

Samples were not tested in compression above  $T > 1560$  °C, where the pillar geometry was unstable due to surface diffusion mediated capillary relaxations; see SI Figure S9. As a result, no pillar compressions were performed at higher temperatures. Capillary relaxations, however, can be exploited for in situ sintering and subsequent tensile testing. The rapid interfacial diffusion enables in situ sintering of the pillar and indenter, and the formation of bicrystal boundaries between the two. The flat grain boundaries, whose small defect free area is on average reasonably well-defined by imaging, provide an ideal opportunity to measure single grain boundary fracture strength. We performed more than 50 measurements at



different strain rates between 0.5 and 80 nm s<sup>-1</sup> using the same contact, that is, the same high-angle grain boundary misorientation of 21° about the [1116], as measured from in situ electron diffraction and electron backscatter diffraction; see SI Figure S10. Figure 3 shows example images before and

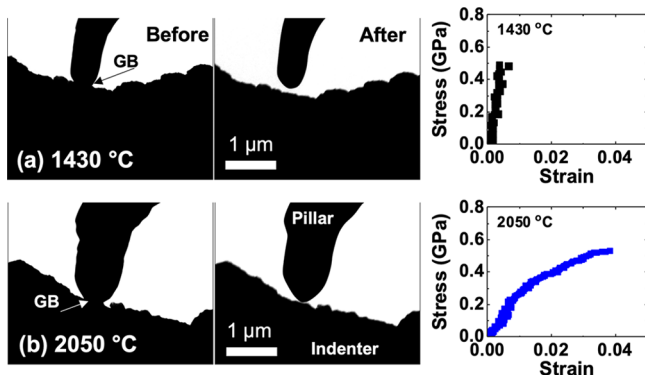


**Figure 3.** Before and after images of in situ TEM tensile testing along with the associated engineering stress–strain curve at different temperatures: (a) 1430 and (b) 2050 °C. The samples were allowed to presinter for ~30 s, which enabled the formation of a grain boundary that subsequently fractures during tensile loading at ~10<sup>-2</sup> s<sup>-1</sup>. Note that due to rapid surface diffusion, the shape of the fractured surface changes after fracture and quickly becomes more rounded.

after brittle fracture as well as associated stress strain curves. Example stress–strain curves from a series of experiments performed at different strain rates at 1930 °C are shown in SI Figure S11. The strain rate affects whether plasticity occurred within the grain boundary, that is, presumably from the motion grain boundary disconnections. A detailed analysis of the mechanism for this grain boundary plastic response is outside the scope of the current Letter and is the subject of an ongoing investigation. On average, the strain rate had negligible effect on the brittle fracture strength outside of an experimental error, that is, standard deviation of approximately 0.1 GPa. The average values along with standard deviation are plotted in Figure 2. Tensile grain boundary fracture performed between ~1430 and 2050 °C also exhibits a weak temperature dependence. The ideal brittle grain boundary work of adhesion relates to the relative grain boundary energy,  $\gamma_{gb}$ , and surface energy,  $\gamma_s$ , through  $W_{ad} = 2\gamma_s - \gamma_{gb}$ . Prior measurements of  $\gamma_{gb}/\gamma_s$  in cubic-stabilized zirconia also produce a weak temperature dependence consistent with our results.<sup>37</sup> On average, the grain boundary fracture strength is 0.5 ± 0.1 GPa. These results demonstrate that performing laser heating based in situ nanomechanical testing enables reliable mechanical testing well into the ultrahigh-temperature regime. At higher temperatures ( $T > 2200$  °C), the sample's vaporization rate increased considerably and affected the sample's geometric stability (see SI Figure S12); higher temperatures were not tested. However, no inherent temperature constraints on the general methodology are anticipated outside of sample stability. Thus, this method is anticipated to provide more routine measurements of ultrahigh-temperature mechanical properties that are currently of limited availability and as a result supports the development of novel ultrahigh-temperature materials.

## CONCLUSIONS

We performed nanomechanical testing of initially nanograined 10 mol % Sc<sub>2</sub>O<sub>3</sub>-stabilized ZrO<sub>2</sub> during in situ TEM imaging

and laser heating. Rapid softening observed between 770 and 960 °C is primarily attributed to grain growth, since preannealed samples exhibited strength comparable to those tested at  $T > 960$  °C. Outside of this temperature range, softening occurs at a rate of ~1.1–1.2 MPa K<sup>-1</sup>. The results indicate that size-dependent room-temperature softening of nanograined oxides, that is, inverse Hall-Petch, is not the result of thermal creep at room temperature in this system. Single grain boundary tensile fracture measurements were performed between 1430 and 2050 °C and an approximately constant fracture strength of ~0.5 ± 0.1 GPa was obtained. Overall, the experiments performed between 25 and 2050 °C demonstrate how laser heating combined with small scale nanomechanical testing enables testing over a broad temperature range extended to the ultrahigh-temperature regime.

## METHODS

Nanostructured powders synthesized by reverse-strike coprecipitation method were calcined at 450 °C for 12 h. Further synthesis information can be found elsewhere.<sup>38</sup> Prior to sintering, powders were degassed under high vacuum (0.08 mmHg) at 400 °C (Smart VacPrep, Micromeritics) to eliminate residual adsorbed water. The degassed powders were stored in a glovebox under high purity Ar atmosphere. A deformable-punch, WC-6% Co alloy, spark plasma sintering (DP-SPS) setup was assembled into the glovebox and quickly inserted into the SPS (Sumitomo Coal Mining Co., Model 1050).

Dense samples (>99%) of 10% Sc<sub>2</sub>O<sub>3</sub>-stabilized ZrO<sub>2</sub> (10ScSZ) with average grain size  $d \approx 9$  nm were produced following the heating schedule outlined in SI Figure S13.<sup>31</sup> SI Figure S14 presents example TEM micrographs and X-ray diffraction patterns from the resulting 10ScSZ.

10ScSZ samples were placed on Cu mounts designed for a Bruker PI-95 nanomechanical tester and coated with Au–Pd. Approximately square cross-section nanograin nanopillars, 500 nm × 500 nm × 600 nm, were prepared by 30 kV Ga<sup>+</sup> ion beam milling (FEI company, Scios 2). A custom indenter tip was fabricated from single crystal 8% Y<sub>2</sub>O<sub>3</sub>-stabilized ZrO<sub>2</sub>. A small piece of 8YSZ was attached to a Ti mount using high-temperature carbon paste (Pelco) coated by C and milled by FIB into a flat punch geometry. Samples were also preannealed in situ in the TEM at ~2050 °C using laser heating methods described below, which heat over an area of ~100 μm. The preannealed regions were then used to prepare coarse grain nanopillars in the FIB, which could subsequently be tested in situ under laser heating. Approximately 100 μm<sup>2</sup> regions surrounding the nanopillars and the indenter tip were coated in FIB deposited Pt to promote local optical absorption; see SI Figure S15. At 1560 °C, small particles are observed on the pillar surface. Ex situ imaging and energy dispersive spectroscopy of these particles suggest that they are primarily Pt that transported, possibly through the vapor phase, onto the pillars; see SI Figure S16. SI Figure S17 shows example SEM micrographs of the indenter and pillars. The crystallographic orientation of the YSZ indenter was measured using electron backscatter diffraction in an SEM; see SI Figure S10. Two-dimensional finite element method simulations were performed using ABAQUS 6.14.

A  $\lambda = 1064$  nm 20 W laser with an ~100 μm spot size was aligned collinearly with the electron beam. Samples were tested under compression at a loading rate of 5 nm s<sup>-1</sup> and with tension rates between 0.5 and 80 nm s<sup>-1</sup>. Samples were

irradiated at constant laser power and a repetition rate of 33 kHz. The samples were held at a given laser power for tens of minutes to allow the sample to stabilize, which was assumed to occur when thermal drift ceased to be observable. Since this time constant for thermal relaxation is several orders of magnitude larger than the laser repetition time constant, the temperature is anticipated to reach a constant steady-state. Pillar compressions were performed using a Bruker PI-95 picoindenter at a constant loading rate of 5 nm s<sup>-1</sup> at a data acquisition rate of ~200 Hz. In situ imaging and diffraction were obtained from the JEOL 2100 using a Tietz video and image processing system at an acquisition rate of ~16 frames per second. Diffraction patterns were measured as a function of laser power after heating to the maximum temperature; that is, the grains were precoarsened such that single crystals could be measured. Diffraction patterns were obtained under identical imaging and diffraction conditions as a function of laser power, and the *d*-spacings were measured for the same single crystalline reflections in each pattern. This helps limit errors in the measurement imposed by aberrations that can distort the shape of the pattern. Experimental measurements of thermal expansion in refs 39 and 40 provide the basis for our temperature calibration. It should be noted that Sc<sub>2</sub>O<sub>3</sub> should exsolve from solution at higher temperatures and could affect the apparent coefficient of thermal expansion. Thus, we anticipate that the lattice parameter-based measurement could overestimate the temperature at higher laser powers. The β-to-cubic phase transition was used as a temperature reference at the lower end of the scale, since the cubic phase was primarily utilized to calibrate high temperatures. Ex situ furnace anneals between 950 and 1700 °C were utilized to coarsen the grains. These data were compared to grain sizes resulting from in situ heating. Additionally, needle samples were prepared to have diameters similar to the pillars and were furnace annealed at different temperatures up to 1700 °C (SI Figure S9). The onset of surface diffusion-mediated capillary relaxations that produce pillar shape changes measured ex situ are also compared with observations made in situ.

## ■ ASSOCIATED CONTENT

### SI Supporting Information


The Supporting Information is available free of charge at <https://pubs.acs.org/doi/10.1021/acs.nanolett.9b04205>.

Additional figures and references (PDF)

## ■ AUTHOR INFORMATION

### Corresponding Authors

**Khalid Hattar** – Sandia National Laboratories,  
Albuquerque, New Mexico; Email: [khattar@sandia.gov](mailto:khattar@sandia.gov)

**Shen J. Dillon** – University of Illinois  
Urbana–Champaign, Urbana, Illinois;  [orcid.org/0000-0002-6192-4026](https://orcid.org/0000-0002-6192-4026); Email: [sdillon@illinois.edu](mailto:sdillon@illinois.edu)

### Other Authors

**Robson L. Grosso** – University of Illinois  
Urbana–Champaign, Urbana, Illinois, Energy and  
Nuclear Research Institute - IPEN, São Paulo, Brazil, and  
University of California - Davis, Davis, California;  
 [orcid.org/0000-0003-3191-3040](https://orcid.org/0000-0003-3191-3040)

**Eliana N. S. Muccillo** – Energy and Nuclear Research  
Institute - IPEN, São Paulo, Brazil

**Dereck N. F. Muche** – University of California - Davis,  
Davis, California

**Gowtham S. Jawahararam** – University of Illinois  
Urbana–Champaign, Urbana, Illinois

**Christopher M. Barr** – Sandia National Laboratories,  
Albuquerque, New Mexico

**Anthony M. Monterrosa** – Sandia National  
Laboratories, Albuquerque, New Mexico

**Ricardo H. R. Castro** – University of California - Davis,  
Davis, California;  [orcid.org/0000-0002-7574-7665](https://orcid.org/0000-0002-7574-7665)

Complete contact information is available at:  
<https://pubs.acs.org/10.1021/acs.nanolett.9b04205>

## Notes

The authors declare no competing financial interest.

## ■ ACKNOWLEDGMENTS

Support from National Science Foundation under Grant DMR 1922867 is acknowledged by S.J.D. R.G. and E.M. gratefully acknowledge FAPESP (2016/06205-1 and 2017/25501-3), CAPES (Finance code 001), and CNPq (305889/2018-4) for financial support. D.M. acknowledges CNPq (236631/2012-8). Support from the Army Research Office Grants W911NF1810361 and W911NF1710026 are acknowledged by R.C. This work was carried out in part in the Frederick Seitz Materials Research Laboratory Central Research Facilities, University of Illinois at Urbana–Champaign. C.M.B. and K.H. were supported by the DOE-BES Materials Science and Engineering Division under FWP 15013170. This work was performed, in part, at the Center for Integrated Nanotechnologies, an Office of Science User Facility operated for the U.S. Department of Energy (DOE) Office of Science. Sandia National Laboratories is a multimission laboratory managed and operated by National Technology and Engineering Solutions of Sandia, LLC, a wholly owned subsidiary of Honeywell International, Inc., for the U.S. DOE's National Nuclear Security Administration under contract DE-NA-0003525. The views expressed in the article do not necessarily represent the views of the U.S. DOE or the United States Government.

## ■ REFERENCES

- (1) Fahrenholtz, W. G.; Hilmas, G. E. Ultra-high temperature ceramics: materials for extreme environments. *Scr. Mater.* **2017**, *129*, 94–99.
- (2) Wuchina, E.; Opila, E.; Opeka, M.; Fahrenholtz, W.; Talmy, I. UHTCs: ultra-high temperature ceramic materials for extreme environment applications. *Electrochem. Soc. Interface* **2007**, *16*, 30–36.
- (3) Monteverde, F.; Bellosi, A.; Scatteia, L. Processing and properties of ultra-high temperature ceramics for space applications. *Mater. Sci. Eng., A* **2008**, *485*, 415–421.
- (4) Mills-Brown, J.; Potter, K.; Foster, S.; Batho, T. The development of a high temperature tensile testing rig for composite laminates. *Composites, Part A* **2013**, *52*, 99–105.
- (5) Bale, H. A.; et al. Real-time quantitative imaging of failure events in materials under load at temperatures above 1,600 °C. *Nat. Mater.* **2013**, *12*, 40–46.
- (6) Hu, P.; Wang, Z. Flexural strength and fracture behavior of ZrB<sub>2</sub>-SiC ultra-high temperature ceramic composites at 1800 °C. *J. Eur. Ceram. Soc.* **2010**, *30*, 1021–1026.
- (7) Neuman, E. W.; Hilmas, G. E.; Fahrenholtz, W. G. Mechanical behavior of zirconium diboride–silicon carbide–boron carbide ceramics up to 2200 °C. *J. Eur. Ceram. Soc.* **2015**, *35*, 463–476.

- (8) Zapata-Solvas, E.; Gómez-García, D.; Domínguez-Rodríguez, A.; Lee, W. E. High temperature creep of 20 vol% SiC-HfB<sub>2</sub> UHTCs up to 2000 °C and the effect of La<sub>2</sub>O<sub>3</sub> addition. *J. Eur. Ceram. Soc.* **2018**, *38*, 47–56.
- (9) Perepezko, J. H. The hotter the engine, the better. *Science (Washington, DC, U. S.)* **2009**, *326*, 1068–1069.
- (10) Kamata, S. Y.; et al. Ultrahigh-temperature tensile creep of TiC-reinforced Mo-Si-B-based alloy. *Sci. Rep.* **2018**, *8*, 10487.
- (11) Gianola, D. S.; Eberl, C. Micro- and nanoscale tensile testing of materials. *JOM* **2009**, *61*, 24–35.
- (12) Cho, J.; et al. In-situ high temperature micromechanical testing of ultrafine grained yttria-stabilized zirconia processed by spark plasma sintering. *Acta Mater.* **2018**, *155*, 128–137.
- (13) Greer, J. R.; De Hosson, J. T. M. Plasticity in small-sized metallic systems: intrinsic versus extrinsic size effect. *Prog. Mater. Sci.* **2011**, *56*, 654–724.
- (14) Wang, L.; et al. Grain rotation mediated by grain boundary dislocations in nanocrystalline platinum. *Nat. Commun.* **2014**, *5*, 4402–4408.
- (15) Zheng, H.; et al. Discrete plasticity in sub-10-nm-sized gold crystals. *Nat. Commun.* **2010**, *1*, 144–151.
- (16) Torrents Abad, O.; Wheeler, J. M.; Michler, J.; Schneider, A. S.; Arzt, E. Temperature-dependent size effects on the strength of Ta and W micropillars. *Acta Mater.* **2016**, *103*, 483–494.
- (17) Best, J. P.; et al. Reversible, high temperature softening of plasma-nitrided hot-working steel studied using in situ micro-pillar compression. *Mater. Sci. Eng., A* **2017**, *680*, 433–436.
- (18) Yang, L. W.; et al. Mechanical properties of metal-ceramic nanolaminates: effect of constraint and temperature. *Acta Mater.* **2018**, *142*, 37–48.
- (19) Messerschmidt, U.; Bartsch, M. High-temperature straining stage for in situ experiments in the high-voltage electron microscope. *Ultramicroscopy* **1994**, *56*, 163–171.
- (20) Baufeld, B.; Messerschmidt, U.; Bartsch, M.; Baither, D. Plasticity of cubic zirconia between 700°C and 1150°C observed by macroscopic compression and by in situ tensile straining tests. *Key Eng. Mater.* **1995**, *97–98*, 431–436.
- (21) Clément, N.; Benyoucef, M.; Legros, M.; Caron, P.; Coujou, A. In situ deformation at 850°C of standard and rafted microstructures of nickel base superalloys. *Mater. Sci. Forum* **2006**, *509*, 57–62.
- (22) Etsell, T. H.; Flengas, S. N. Electrical properties of solid oxide electrolytes. *Chem. Rev.* **1970**, *70*, 339–376.
- (23) Evans, A. G.; Clarke, D. R.; Levi, C. G. The influence of oxides on the performance of advanced gas turbines. *J. Eur. Ceram. Soc.* **2008**, *28*, 1405–1419.
- (24) Kuriakose, A. K.; Margrave, J. L. The oxidation kinetics of zirconium diboride and zirconium carbide at high temperatures. *J. Electrochem. Soc.* **1964**, *111*, 827–831.
- (25) Arachi, Y. Electrical conductivity of the ZrO<sub>2</sub>–Ln<sub>2</sub>O<sub>3</sub> (Ln = lanthanides) system. *Solid State Ionics* **1999**, *121*, 133–139.
- (26) Jacobson, A. J. Materials for solid oxide fuel cells. *Chem. Mater.* **2010**, *22*, 660–674.
- (27) Boldrin, P.; Brandon, N. P. Progress and outlook for solid oxide fuel cells for transportation applications. *Nat. Catal.* **2019**, *2*, 571–577.
- (28) Ryou, H.; et al. Below the Hall-Petch limit in nanocrystalline ceramics. *ACS Nano* **2018**, *12*, 3083–3094.
- (29) Karch, J.; Birringer, R.; Gleiter, H. Ceramics ductile at low temperature. *Nature* **1987**, *330*, 556–558.
- (30) Cho, J.; et al. High temperature deformability of ductile flash-sintered ceramics via in-situ compression. *Nat. Commun.* **2018**, *9*, 2063–2071.
- (31) Grosso, R. L.; et al. Sintering of translucent and single-phase nanostructured scandia-stabilized zirconia. *Mater. Lett.* **2019**, *253*, 246–249.
- (32) Hattar, K.; Bufford, D. C.; Buller, D. L. Concurrent in situ ion irradiation transmission electron microscope. *Nucl. Instrum. Methods Phys. Res., Sect. B* **2014**, *338*, 56–65.
- (33) Niekietl, F.; Kraschewski, S. M.; Müller, J.; Butz, B.; Spiecker, E. Local temperature measurement in TEM by parallel beam electron diffraction. *Ultramicroscopy* **2017**, *176*, 161–169.
- (34) Badwal, S. P. S.; Ciacchi, F. T.; Milosevic, D. Scandia–zirconia electrolytes for intermediate temperature solid oxide fuel cell operation. *Solid State Ionics* **2000**, *136–137*, 91–99.
- (35) Evans, P. E. Creep in yttria- and scandia-stabilized zirconia. *J. Am. Ceram. Soc.* **1970**, *53*, 365–369.
- (36) Camposilvan, E.; Anglada, M. Size and plasticity effects in zirconia micropillars compression. *Acta Mater.* **2016**, *103*, 882–892.
- (37) Tsoga, A.; Nikolopoulos, P. Surface and grain-boundary energies in yttria-stabilized zirconia (YSZ-8 mol%). *J. Mater. Sci.* **1996**, *31*, 5409–5413.
- (38) Grosso, R. L.; Muccillo, E. N. S.; Castro, R. H. R. Phase stability in scandia-zirconia nanocrystals. *J. Am. Ceram. Soc.* **2017**, *100*, 2199–2208.
- (39) Mizutani, Y.; Tamura, M.; Kawai, M.; Yamamoto, O. Development of high-performance electrolyte in SOFC. *Solid State Ionics* **1994**, *72*, 271–275.
- (40) Singh, R. N.; Chavan, S. V. Processing and properties of scandia-doped zirconia electrolyte for intermediate temperature SOFC. *ECS Trans* **2007**, *7*, 2207–2212.